Anal. Bioanal. Electrochem., Vol. 17, No. 8, 2025, 677-695
https://www.doi.org/10.22034/abec.2025.733510

Analytical & Bioanalytical Electrochemistry

Full Paper

Design and Electrochemical Evaluation of Cu/Cu_2O–SGr–Bi_2S_3 Nanohybrids for Enhancing CO_2 Electroreduction

Ahmad Rouhollahi, Maral Fouladvand, and Elaheh Bakhshi

Department of Analytical Chemistry, Faculty of Chemistry, K.N. Toosi University of Technology, 15418-49611, Tehran, Iran

*Corresponding Author, Tel.: (+98) 23064222
E-Mail: rouhollahi@kntu.ac.ir

Received: 28 August 2025 / Received in revised form: 14 October 2025/ Accepted: 20 October 2025 / Published online: 31 December 2025

Abstract- The electrochemical conversion of carbon dioxide (CO_2) represents a promising strategy for reducing greenhouse gas emissions and facilitating sustainable chemical production. Here, we present a rationally engineered copper foam electrode integrated with a multifunctional nanohybrid comprising copper oxide (Cu_2O), bismuth sulfide (Bi_2S_3), and sulfur-doped graphene (SGr–Bi_2S_3). The Cu/Cu_2O–SGr–Bi_2S_3 composite leverages synergistic electronic and catalytic interfaces, resulting in outstanding electrocatalytic performance for CO_2 reduction. Comprehensive physicochemical and electrochemical analyses, including cyclic voltammetry, chronoamperometry, and electrochemical impedance spectroscopy, demonstrate that the hybrid electrodes deliver significantly higher cathodic current densities and exhibit markedly reduced charge transfer resistance under CO_2-saturated conditions compared to unmodified copper counterparts. The nanoscale distribution of Bi_2S_3 effectively increases the density of active catalytic sites, while strong electronic coupling at the heterointerfaces suppresses the competing hydrogen evolution reaction. As a result, the Cu/Cu_2O–SGr–Bi_2S_3 nanohybrids achieve superior activity, enhanced current densities, and excellent operational stability, outperforming conventional copper-based electrodes. These results position the Cu/Cu_2O–SGr–Bi_2S_3 nanohybrids as highly efficient, scalable, and economically viable electrocatalysts for next-generation CO_2 reduction technologies.

Keywords- Electrochemical Characterization; Sulfur-doped graphene; CO_2 reduction; Electrocatalysis; Cu/Cu_2O–SGr–Bi_2S_3 electrodes; Stability

1. INTRODUCTION

The continued rise in anthropogenic CO_2 emissions remains a critical driver of global climate change, underscoring the need for scalable strategies to mitigate atmospheric CO_2 levels [1,2]. Conventional mitigation techniques, predominantly carbon capture and storage, have shown limited efficacy in curtailing the accumulation of CO_2 in the atmosphere [3,4]. Recently, the electrochemical reduction of CO_2 (CO_2RR) has emerged as a promising alternative that enables the direct conversion of CO_2 into valuable chemicals and fuels, supporting circular carbon economy initiatives and the integration of renewable energy sources [5,6]. Nevertheless, the electrochemical conversion of CO_2 remains beset by inherent challenges: the low activation of the CO_2 molecule and the ubiquity of parasitic side reactions, such as the hydrogen evolution reaction (HER), severely limit process efficiency, selectivity, and commercial viability [7-11]. Overcoming these challenges requires the rational design and development of advanced electrocatalysts that can enhance the rate and selectivity of CO_2 reduction while effectively suppressing competing side reactions. Crucial to the viability of this process is the development of robust, earth-abundant catalysts and electrode materials that can achieve high selectivity, activity, and operational stability under mild conditions.

Copper-based materials, particularly Cu_2O, exhibit markedly enhanced electrocatalytic performance owing to their favorable electronic structures and strong interaction with CO_2 reaction intermediates [12-15]. Structured copper foams further augment catalytic performance by providing a large electrochemically active surface area and excellent conductivity, enhancing mass transport and facilitating efficient electron transfer at the electrode–electrolyte interface [16-19]. Despite these advantages, intrinsic limitations such as the instability of Cu_2O under reductive conditions impede long-term operational stability. Consequently, recent research has focused on constructing composite and heterostructured Cu-based electrodes, with particular emphasis on nanoscale engineering and interfacial modulation to promote charge separation and maximize surface reactivity [20-24].

Incorporating bismuth-based phases has proven especially advantageous, as bismuth offers high selectivity for CO_2RR in aqueous environments while intrinsically suppressing HER, thanks to its high HER overpotential and environmental benignity [25,26]. The combination of bismuth species with high-conductivity carbon frameworks, such as sulfur-doped graphene, not only improves catalyst dispersion but also enhances the electronic conductivity and stability of the hybrid system [27-30]. When judiciously combined with highly conductive materials such as graphene, bismuth-based electrocatalysts exhibit notable improvements in catalytic efficiency and operational stability under electrochemical conditions. Furthermore, the incorporation of advanced carbonaceous materials such as graphene has proven transformative in the domain of electrocatalyst design. Graphene, with its extraordinary electrical conductivity, remarkable chemical inertness, and ultrahigh specific surface area, provides a versatile scaffold for stabilizing atomically dispersed metal species, facilitating rapid electron

transfer, and markedly boosting both current density and product selectivity in CO_2 electroreduction [2,31,32].

Nevertheless, pristine graphene's inert basal plane and weak CO_2 adsorption can limit its catalytic efficacy, prompting the need for deliberate structural and chemical modifications. Heteroatom doping especially with sulfur has emerged as a powerful route to engineer the graphene lattice, introduce abundant defect sites, and tailor the local electronic environment for enhanced CO_2 activation [33,34]. Incorporation of sulfur atoms generates C–S bonds and thiophene-like moieties at edge and vacancy sites, which induce charge polarization, create electron-rich centers, and modulate spin density distributions. Beyond chemical functionalization, nanoscale architectural engineering such as constructing three-dimensional porous networks, bilayer composites, or hierarchically stacked frameworks dramatically increases the density of accessible active sites, optimizes mass and ion transport, and reinforces structural stability under prolonged operation. Surface defect modulation and targeted functionalization strategies synergize with these architectures to suppress the competing hydrogen evolution reaction, extend catalyst lifetime, and maintain high selectivity over extended electrolysis periods. Collectively, the strategic integration of sulfur-doped graphene supports with copper-based electrocatalysts paves a clear pathway toward practical, scalable, and sustainable CO_2RR technologies, delivering exceptional activity, durability, and product specificity.

In this study, we further this progress by designing and systematically characterizing a new class of copper-based electrodes, co-engineered with bismuth and graphene derivatives as synergistic dopants. Comprehensive analyses of morphology, crystal structure, and electrochemical properties are employed to unveil the mechanisms underlying improved catalytic activity, enhanced charge separation, and prolonged operational stability. These results offer new mechanistic insights and design principles for the rational development of efficient, scalable, and robust electrocatalysts for CO_2 electroreduction, advancing the broader application of sustainable CO_2 utilization technologies.

2. EXPERIMENTAL SECTION

2.1. Chemicals and Reagents

Graphite powder, sodium nitrate ($NaNO_3$), sulfuric acid (H_2SO_4, 98%), sulfanilic acid (SA, $C_6H_7NO_3S$), copper sulfate pentahydrate ($CuSO_4 \cdot 5H_2O$), sodium hydroxide (NaOH), nitric acid (HNO_3), and hydrochloric acid (HCl, 37%) were purchased from Merck (Germany). Sodium nitrite ($NaNO_2$) and potassium permanganate ($KMnO_4$, 99%) were supplied by Scharlau (Spain). Hydrogen peroxide (H_2O_2) was purchased from Iran. Bismuth(III) nitrate pentahydrate ($Bi(NO_3)_3 \cdot 5H_2O$) and lactic acid (solvent) were provided by Sigma-Aldrich (USA). Deionized water was used as the solvent for all aqueous solutions. Nitrogen (N_2) and carbon dioxide (CO_2) gases with 99.9% purity were sourced from the Farafan gas production

facility in Iran. A three-electrode system was used, consisting of a platinum wire counter electrode, a silver/silver chloride (Ag/AgCl; 3.5 M KCl) reference electrode, and a copper foam (Cu foam) working electrode. Commercial Cu foam with dimensions of 1×1 cm and 59% porosity and 0.49-0.4 mm thickness (purchased from Redox Kala Company) was used as the substrate. Prior to electrodeposition, the Cu foam working electrodes were cleaned ultrasonically by sequential sonication in acetone, ethanol, and distilled water for 10 minutes each. All chemicals were used without further treatment, except where explicitly mentioned.

2.2. Electrodeposition of p-Cu_2O Layer

A layer of p-Cu_2O electrode was deposited using a solution containing 0.5 M $CuSO_4 \cdot 5H_2O$ and 3 M lactic acid. The deposition process was conducted at a temperature of 60°C. To determine the most effective electrocatalyst for the electrochemical reduction of CO_2, several parameters were optimized including: pH, voltage, coulomb, and concentration. The detailed optimization procedures and results for these parameters will be discussed in the results section.

2.3. Synthesis of GO

To synthesize GO using the modified Hummers method [35,36], H_2SO_4 (60 mL) was poured into a large beaker and placed in an ice bath. Then, graphite (2 g) and $NaNO_3$ (1 g) were added to the beaker and stirred for 2 h. During the reaction, the temperature was kept below 4 °C. In the next step, $KMnO_4$ (6 g) was carefully added to the mixture as a strong oxidizing agent. Afterward, the ice bath was removed, the temperature was raised to 38 °C, and the solution was stirred for 12 h by a magnetic stirrer. Then, water was added slowly to the mixture, and after 15 min stirring while the temperature increased up to 98 °C, H_2O_2 (12 mL) was poured into the beaker. Finally, the obtained GO was repeatedly centrifuged and washed with diluted HCl and distilled water until the pH reached around 6. The final dispersion of GO was dried at room temperature.

2.4. Preparation of SGr-Bi_2S_3

The synthesized composite SGr-Bi_2S_3 was prepared via a simple method. Initially, 13 mL of a 10 mM solution of $Bi(NO_3)_3 \cdot 5H_2O$ was combined with 2 mL of a graphene oxide (GO) suspension (25 mg in 5 mL of water). Subsequently, 540.4 mg of $Na_2S \cdot 5H_2O$ (150 mM) was added dropwise into the mixture under continuous stirring to ensure homogeneous incorporation of the sulfur source. The reaction mixture was then transferred to a Teflon-lined stainless-steel autoclave and subjected to hydrothermal treatment at 180°C for 3 hours. Following the completion of the reaction, the resulting black precipitate was collected via centrifugation and thoroughly washed with double-distilled water to remove by-products or unreacted reagents. The purified SGr-Bi_2S_3 composite was air-dried at room temperature and

stored in a moisture-free container for further use [37]. To prepare an optimized electrocatalyst ink, 4 mg of the synthesized SGr-Bi_2S_3 material was precisely weighed and uniformly dispersed in a solvent mixture comprising 50 µL of distilled water, 50 µL of absolute ethanol, and 10 µL of Nafion solution using ultrasonic agitation to ensure homogeneity. The prepared catalyst ink was applied to the working electrode, which had a copper oxide layer electrochemically deposited onto its surface. The electrode was firmly positioned on a flat workbench to maintain a horizontal orientation throughout the deposition process. To minimize contamination, the workspace was selected to be free from dust and turbulent airflow. A 10 µL droplet of the electrocatalyst ink was carefully pipetted onto the center of the electrode's surface and allowed to dry completely at ambient temperature, ensuring uniform adhesion of the ink layer. After the drying process, the modified electrode was ready for electrochemical testing and performance evaluation, marking the successful preparation of the SGr-Bi_2S_3-based electrocatalyst system.

2.5. Material Characterization

To investigate the surface morphology of the prepared photocathodes, Field Emission Scanning Electron Microscopy (FESEM) images were obtained using a VEGA3 instrument from TESCAN company. For studying the crystalline structure, X-ray Diffraction (XRD) analysis was performed using a PW1730 instrument from PHILIPS company.

2.6. Electrochemical measurements

All electrochemical experiments were conducted using Metrohm Autolab PGSTAT302N instrument in a three-electrode cell configuration. The setup included a 3.5 M Ag/AgCl electrode as the reference electrode, a platinum plate as the counter electrode, and the prepared photocathodes as the working electrode. The electrochemical performance of the photoelectrode composed of copper composites was examined using linear sweep voltammetry (LSV, Metrohm Autolab PGSTAT302N), cyclic voltammetry (CV), chronoamperometry, and electrochemical impedance spectroscopy (EIS, Metrohm Autolab PGSTAT302N). To assess the stability of the photoelectrode composites, chronoamperometry was conducted by applying a constant potential of -1 V Vs Ag/AgCl on electrochemical cells. The electron transfer kinetics was evaluated using EIS with an open circuit potential (OCP) of 10 mV and a frequency range from 0.1 to 100.000 Hz.

3. RESULTS AND DISCUSSION

All optimization steps in this study were systematically designed and rigorously implemented to yield the most efficient Cu_2O electrocatalyst for electrochemical CO_2RR. The experimental strategy was predicated on maximizing both catalytic current density and

operational stability. To identify the optimal Cu^{2+} precursor concentration for the synthesis of catalytically active Cu_2O, copper(II) sulfate pentahydrate was dissolved in lactic acid at concentrations of 0.25, 0.50, and 0.75 M, while all other variables were stringently controlled.CV measurements were performed in a 0.10 M carbonate buffer at pH≈ 8 under both CO_2 and N_2 atmospheres. As displayed in Figure 1(a, e, and i), the Cu–Cu_2O electrode synthesized using a 0.50 M precursor concentration exhibited a substantially enhanced current density under CO_2, relative to electrodes fabricated at alternative concentrations and compared to the N_2 control. This observation indicates that a 0.50 M precursor optimally balances nucleation and growth, resulting in a Cu_2O surface enriched with catalytically accessible active sites, while effectively suppressing parasitic side reactions. Both lower and higher concentrations led to suboptimal nucleation or excessive particle aggregation, respectively, collectively diminishing the number and accessibility of active catalytic sites and thereby attenuating CO_2RR efficiency.

Precise modulation of the electrolyte pH during Cu_2O synthesis proved critical in tuning the catalyst's surface chemistry and electronic structure. As evidenced by the CV results in Figure 1(b and j), the highest catalytic current density and the most pronounced CO_2RR enhancement (relative to the N_2 background, Figure 1f) were achieved at pH ≈ 12. This improvement is plausibly attributed to a greater abundance of OH^- ions, which facilitate the preferential formation of catalytically favorable Cu^+ surface states.

The electrodeposition potential exerted a decisive influence on the morphological and electronic properties of the resulting Cu_2O films [38]. Systematic variation of the applied potential (–0.30, –0.40, and –0.50 V vs. Ag/AgCl) demonstrated that –0.40 V was optimal for engineering uniform, nanostructured Cu_2O layers characterized by high electrocatalytic activity (Figure 1c, 1g). More negative potentials (e.g., –0.50 V) did not further improve, and in some instances diminished, the current density, likely owing to increased ohmic losses or deleterious side reactions [39]. The total charge applied during electrodeposition governed both the resultant film thickness and electrochemically active surface area. As presented in Figure 1(d and h), increasing the deposition charge to –0.6 C maximized the catalytic current density for CO_2RR, indicative of optimal surface coverage by catalytically relevant Cu_2O nanostructures. Application of higher charges (e.g., –0.8 C; see Figure 1l) generated excessively thick, compact films, which impeded mass transport, reduced accessibility to catalytic sites, and consequently depressed overall efficiency, most likely due to increased resistance and a potential decline in selectivity. Therefore, an applied deposition charge of –0.6 C was determined to establish the optimal balance between maximizing catalytic surface area and mitigating diffusion limitations, resulting in the most active and robust Cu_2O electrocatalyst for CO_2RR developed in this study.

As shown in Figure 2(a–f), FESEM was systematically utilized to elucidate the morphological evolution of the synthesized materials. A comparative analysis was performed

on three principal systems: Cu/Cu_2O, SGr–Bi_2S_3, and the hybrid Cu–Cu_2O/SGr–Bi_2S_3 composite, to explicitly assess the impact of composite integration on surface architecture and hierarchical structuring.

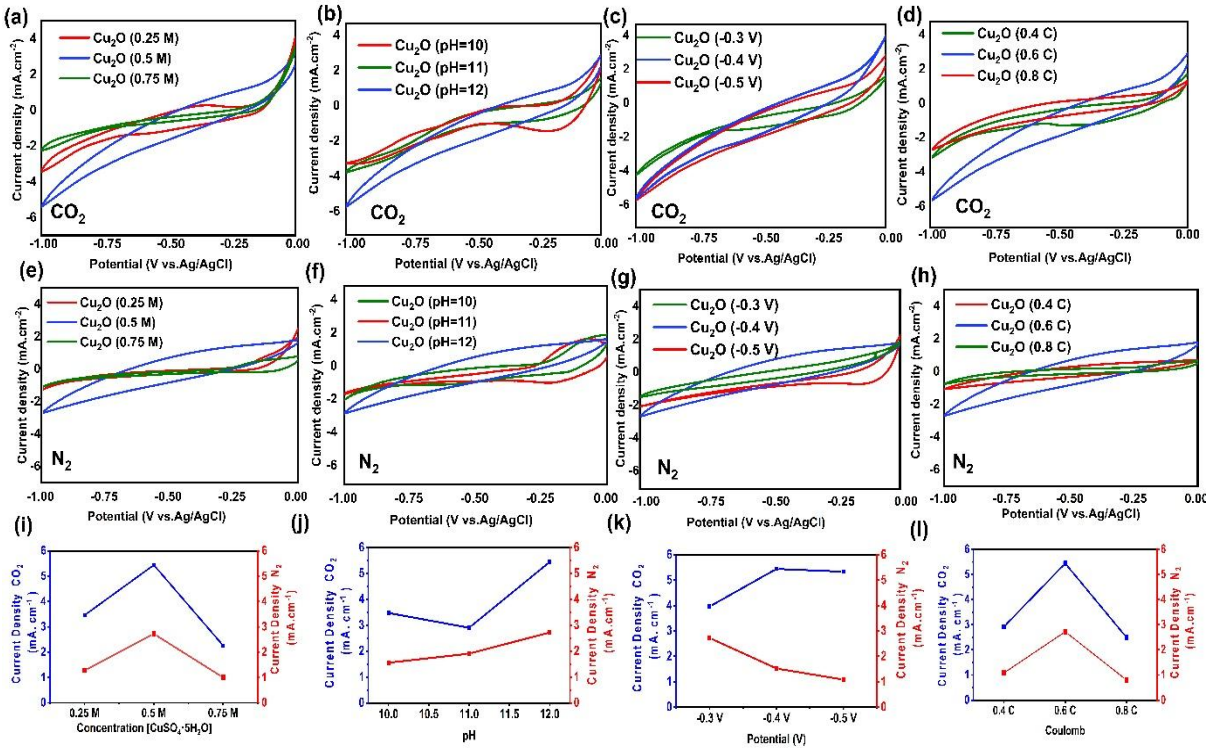

Figure 1. Optimization of electrodeposition conditions for Cu_2O under different atmospheres: (a–d) electrodeposition behaviors in CO_2-saturated electrolyte; (e–h) electrodeposition behaviors in N_2-saturated electrolyte; (i–l) corresponding current responses obtained in electrolytes saturated with CO_2 and N_2

The FESEM micrograph of the pristine copper foam substrate (Figure 2a) reveals a characteristically smooth and largely featureless topology, representative of its unmodified state. Upon electrochemical deposition, the Cu/Cu_2O electrode (Figure 2b–d) displays a significant transformation uniformly roughened surfaces densely populated by spheroidal and compact Cu_2O particulates. This rough morphology is evidence of the effective nucleation and growth of Cu_2O domains achieved via a controlled synthetic protocol. Notably, with increasing magnification (Figure 2c, d), the Cu_2O particulates are seen to aggregate into clusters, forming a dense and homogeneously distributed layer across the copper substrate. This microstructural evolution, especially under strongly alkaline conditions (pH ≈ 12 during deposition), correlates well with reports of electrochemically active Cu-based catalysts optimized for CO_2 reduction in alkaline regimes [40]. The SGr–Bi_2S_3 system is depicted at progressively higher magnifications in panels (Figure 2f–h). The low-magnification image (Figure 2f) shows a relatively continuous film with granular features. As the magnification increases (Figure 2g,

h), this morphology evolves into densely packed nanoscale domains, exhibiting three-dimensional stacking and surface-parallel planes characteristic of sulfonated graphene sheets supporting hierarchical Bi_2S_3 assemblies. These superstructures are expected to substantially increase the electrochemically accessible surface area, thereby improving both mass transport characteristics and catalyst-reactant interfacial interactions.

Critically, the composite Cu–Cu_2O/SGr–Bi_2S_3 (Figure 2i–l) exhibits a highly disordered, porous, and heterogeneously textured architecture. FESEM analysis reveals that Cu_2O nanoparticles act as nucleation templates, guiding both the spatial distribution and growth orientation of the SGr–Bi_2S_3 domains. The hybrid structure displays intricate encapsulation of Bi_2S_3 nanostructures within the conductive sulfonated graphene network, enhancing the mechanical stability and electronic conductivity of the composite. Panels (Figure 2i–l), spanning from lower to higher magnification, emphasize the composite's hierarchical porosity and the uniform, interconnected dispersion of the constituent nanostructures.

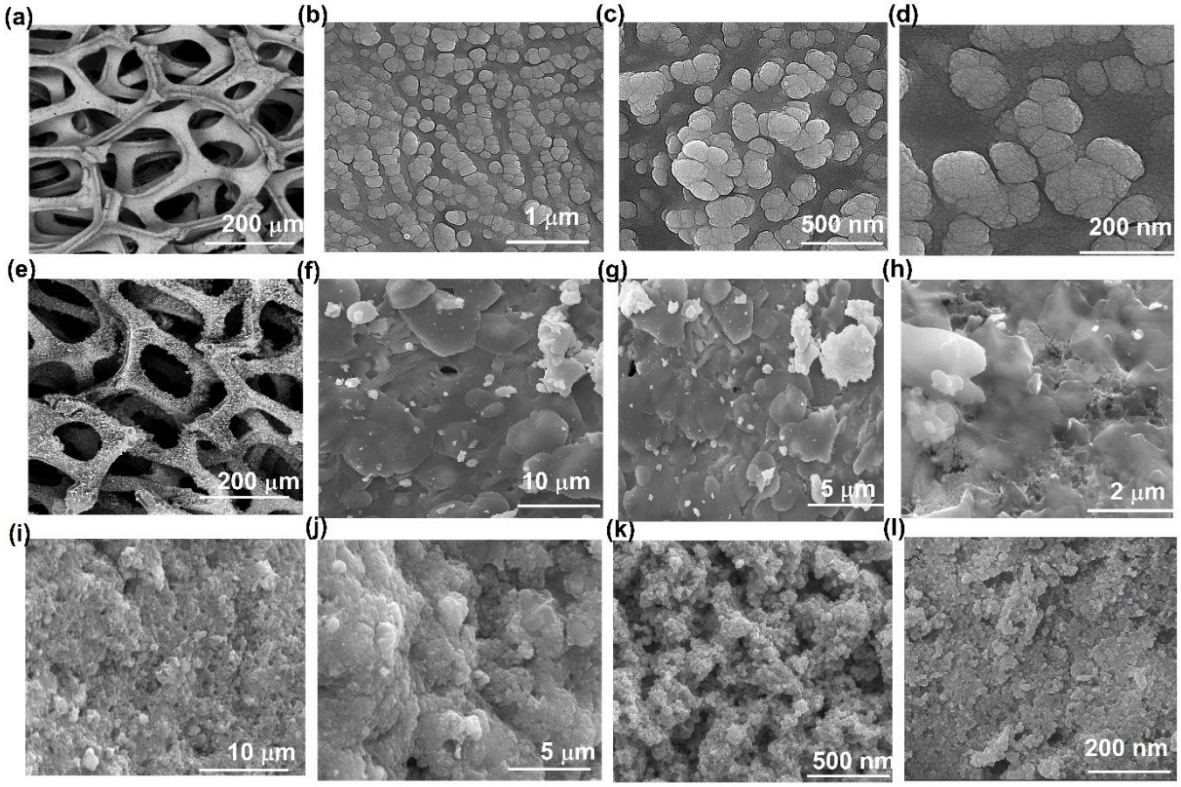

Figure 2. FESEM images of (a) Cu foam bare, (b–d) Cu/Cu_2O electrode, (e–h) SGr–Bi_2S_3 on Cu foam, and (i–l) Cu/Cu_2O/SGr–Bi_2S_3 composite

A side-by-side comparison of Figure 2a (pristine Cu foam) and Figure 2e (composite) underscores the successful surface modification and homogeneous integration of SGr–Bi_2S_3 on the Cu_2O-modified scaffold. This synergy between the components dramatically amplifies both the surface area and the density of catalytically active domains, which is paramount for

facilitating efficient charge transfer and high current densities during electrochemical CO_2 reduction. Overall, the FESEM results robustly support the hybrid material's architectural and physicochemical suitability for advanced electrochemical CO_2RR applications, where abundant active sites, hierarchical porosity, and enhanced electron transfer pathways are critical for catalytic performance.

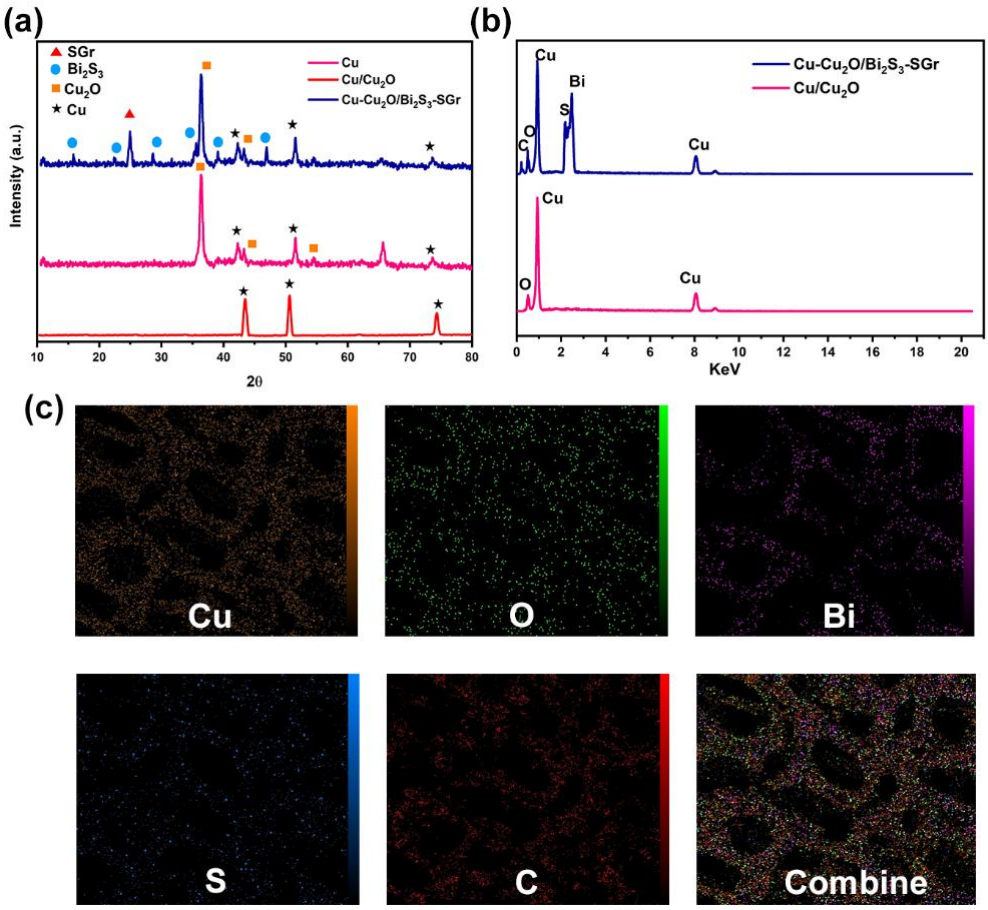

Figure 3. (a) XRD patterns of cathodes. (b) EDS elemental distribution diagram; and (c) Elemental mapping images for the $Cu/Cu_2O–SGr–Bi_2S_3$ cathode

The XRD patterns of the synthesized Cu/Cu_2O nanocomposites, as shown in Figure 3(a), display distinct diffraction peaks at 2θ values of 36.5°, 42.4°, and 61.5°, which correspond to the (111), (200), and (220) planes of Cu_2O (JCPDS no. 05-0667) [41]. Additional peaks at 43.4° and 50.4° are assigned to the (111) and (200) planes of metallic Cu, in agreement with JCPDS no. 04-0836 [41]. The concurrent presence of these peaks confirms the coexistence of both metallic Cu and Cu_2O within the nanocomposite matrix. Following the deposition of SGr-Bi_2S_3 onto the Cu/Cu_2O photoelectrodes, the XRD spectrum exhibits well-defined peaks attributable to both Bi_2S_3 and SGr phases. Characteristic reflections at 15.8°, 22.4°, 24.9°, 28.6°, 31.6°, 35.5°, 39.0°, 43.1°, 46.9°, 48.2°, and 62.5° are indexed to the (020), (220), (130), (211), (040), (240), (041), (250), (350), (060), and (171) planes of Bi_2S_3 nanoparticles,

consistent with standard reference data [37]. Furthermore, a minor diffraction peak observed at 24.9° is ascribed to the (002) plane of SGr, substantiating the successful incorporation of SGr within the Bi_2S_3 matrix and confirming the formation of the Cu/Cu_2O–SGr–Bi_2S_3 heterostructure [37]. These XRD results conclusively demonstrate the successful fabrication of a multi-component photoelectrode capable of promoting synergistic interactions among Cu, Cu_2O, Bi_2S_3, and SGr.

Further supporting evidence is provided by EDX analysis (Figure 3b), which confirms the presence of Cu, C, S, and Bi in the fabricated electrode, verifying the intended elemental composition. Elemental mapping (Figure 3c) reveals a uniform spatial distribution of Cu, O, C, S, and Bi across the electrode surface, highlighting the homogeneous integration of all constituent elements within the composite structure.

As illustrated in Figure 4a, introducing CO_2 into the electrochemical system results in a marked increase in current density across the entire potential window, compared to measurements conducted under a N_2 atmosphere [42]. This pronounced enhancement underscores the superior electrocatalytic activity of the Cu/Cu_2O-SGr-Bi_2S_3 electrode toward CO_2 electroreduction. To objectively compare electrocatalytic performance, the CO_2 reduction activities of the Cu/Cu_2O-SGr-Bi_2S_3, Cu/Cu_2O, and bare Cu foam electrodes were systematically investigated under CO_2-saturated conditions. As depicted in Figure 4 b, incorporation of SGr-Bi_2S_3 nanostructures into the Cu/Cu_2O matrix significantly improves the electrical conductivity and facilitates electron transfer kinetics. This synergistic effect manifests as increased current densities and a more cathodically shifted onset potential for CO_2 reduction on the Cu/Cu_2O-SGr-Bi_2S_3 electrode compared to the reference electrodes [7,26,43]. These electrocatalytic enhancements are corroborated by additional electrochemical characterizations, confirming the outstanding CO_2 reduction capabilities of the composite electrode [42,44,45].

The electrocatalytic CO_2 reduction performances of the Cu/Cu_2O-SGr-Bi_2S_3, Cu/Cu_2O, and bare Cu foam cathodes were systematically investigated using LSV in a conventional three-electrode setup with 0.10 M $KHCO_3$ as the electrolyte. As shown in Figure 4c and d the Cu/Cu_2O electrode achieves a current density of 3.4 mA cm^{-2} under a CO_2 atmosphere comparable to the response observed under N_2 while the removal of CO_2 results in a discernible decrease in current density. This behavior confirms the active role of the Cu_2O component in promoting CO_2 electroreduction [12,44,46].

Distinct differences in CO_2 reduction activity were observed among the three cathode configurations based on their respective LSV profiles (Figure 4c-d). Notably, the Cu/Cu_2O-SGr-Bi_2S_3 electrode demonstrates a more positive onset potential for CO_2 reduction compared to the Cu/Cu_2O electrode. Furthermore, the Cu/Cu_2O-SGr-Bi_2S_3 electrode achieves a current density that is twofold higher than that of the Cu/Cu_2O electrode. This substantial enhancement is primarily attributed to the unique hierarchical architecture and increased porosity introduced

by the SGr-Bi_2S_3 phase (see Figure 2), which markedly increases the effective electroactive surface area. In contrast, the unmodified Cu/Cu_2O electrode possesses a relatively flat morphology, resulting in diminished catalytic activity. These results highlight the pivotal role of rational structural engineering in optimizing CO_2 electroreduction performance.

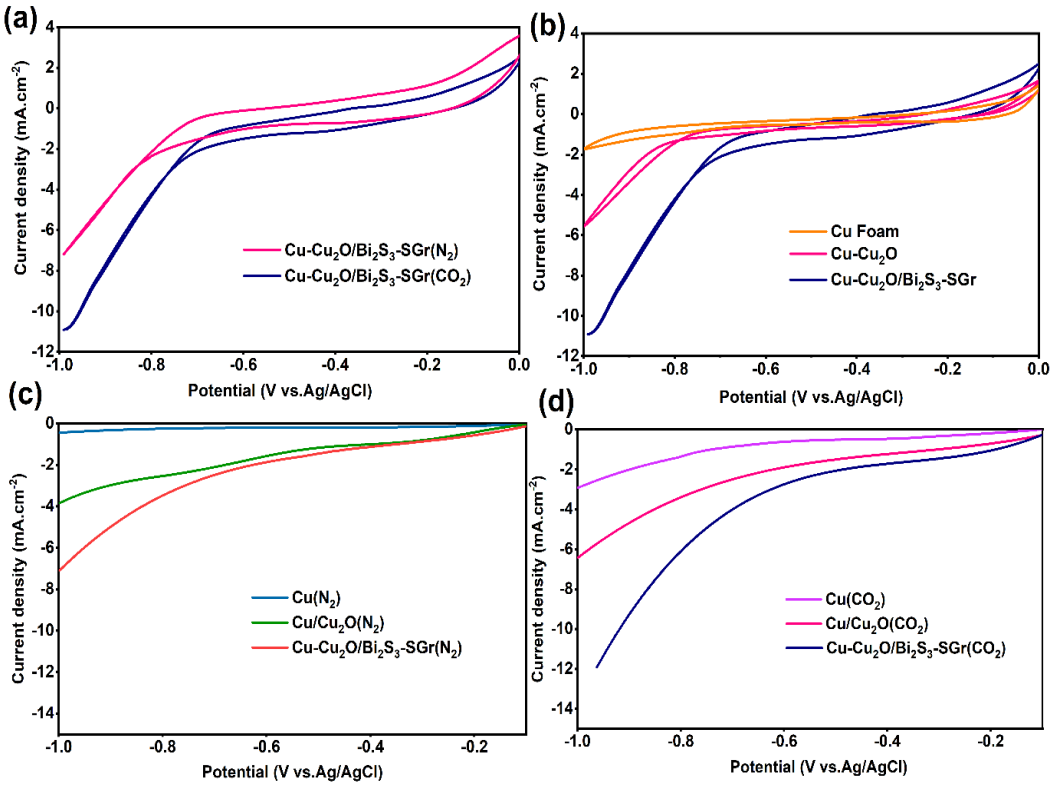

Figure 4. (a) CV curves of the Cu/Cu_2O-SGr-Bi_2S_3 cathode in CO_2- and N_2-saturated electrolytes. (b) CV curves of various cathodes in CO_2-saturated electrolyte. LSV curves of different cathodes in electrolytes saturated with(c) CO_2 and (d) N_2

Electrochemical Impedance Spectroscopy (EIS) is a powerful technique for unraveling the intricate physicochemical processes and interfacial phenomena that govern electrochemical systems [36]. In this study, EIS was systematically employed to interrogate the electrode–electrolyte interface and to elucidate the charge transfer mechanisms operative within various photoelectrode assemblies under reactive conditions. The obtained Nyquist plots (Figure 5a, b) for both Cu/Cu_2O and Cu/Cu_2O-SGr-Bi_2S_3 electrodes, recorded in N_2 and CO_2-saturated electrolytes, provide valuable insights into the dynamic interfacial characteristics and the impact of compositional modifications on electrochemical performance.

Among all tested electrodes, the Cu/Cu_2O-SGr-Bi_2S_3 composite demonstrated the lowest series resistance (R_s), reflecting markedly superior electronic conductivity. This enhancement can be attributed to the robust interfacial contact and the synergistic interaction between the multiple cathode phases and the substrate, yielding more efficient pathways for electron transport. In the Nyquist plots, the diameter of each semicircular arc serves as a diagnostic

measure of the charge transfer resistance (R_{ct}) at the electrode/electrolyte interface [41]. A reduced semicircle radius directly correlates with a lower R_{ct}, signifying more facile charge transfer kinetics. Notably, for all electrodes studied, the semicircle diameter under CO_2-saturated conditions was consistently smaller than under N_2, indicating the promotion of electrocatalytic activity toward CO_2 reduction, particularly for the Cu/Cu_2O-SGr-Bi_2S_3 architecture [6]. To further quantify the impedance characteristics, each electrode configuration was rigorously fitted to an optimized equivalent circuit model, allowing for precise extraction of individual resistance and capacitance parameters (see Figure 5c). The Cu/Cu_2O-SGr-Bi_2S_3 electrode exhibited the smallest R_{ct} among all samples, conclusively highlighting its superior interfacial charge transport properties. This observation is in excellent agreement with the enhanced current densities observed in the corresponding LSV measurements, further affirming that the rational compositional and architectural design of the Cu/Cu_2O-SGr-Bi_2S_3 system results in highly efficient charge transfer dynamics.

The significant reduction in R_{ct} can be ascribed to both the increased density of catalytically active sites, arising from the composite's hierarchical and porous structure and the optimized electronic coupling among the component phases, which together facilitate rapid charge carrier migration toward CO_2 molecules within the electrolyte. Comparative analysis of R_{ct} across all tested substrates underscores the decisive role of electrode composition and interfacial engineering, while Cu-based systems inherently exhibit lower R_{ct} values due to efficient electron mobility, further performance gains are realized through strategic incorporation of SGr-Bi_2S_3, which minimizes interfacial defects and maximizes overall conductive and catalytic efficiency [47]. In contrast, electrodes with intrinsically higher R_{ct}, such as unmodified copper or alternative substrates, suffer from sluggish charge transfer kinetics, typically resulting from limited charge carrier mobility and increased interfacial impedance [48].

Collectively, these EIS findings highlight the critical importance of advanced materials integration and interfacial control in the design of next-generation electrocatalysts for efficient CO_2 reduction [47].

A mechanistic understanding of the electrochemical CO_2 reduction reaction (CO_2RR) was achieved by constructing Tafel plots from LSV data [49]. Comparative analysis of the Tafel slopes provided valuable insights into the reaction kinetics and the underlying catalytic mechanisms. To further evaluate catalytic efficiency, the overpotentials (η) required (see Figure 4c). The Cu–Cu_2O/SGr-Bi_2S_3 catalyst consistently achieved CO_2RR at notably lower overpotentials, confirming its superior catalytic activity and efficiency [50]. The integration of SGr-Bi_2S_3 into the Cu–Cu_2O matrix resulted in a substantial shift of the LSV onset potential towards more positive (less negative) values, indicative of accelerated reaction kinetics. This beneficial effect is attributed to enhanced CO_2 adsorption at the catalyst surface, owing to the unique surface chemistry and high density of active sites introduced by the SGr-Bi_2S_3 component. Analysis of the linear Tafel regions (Figure 6d) underscores the kinetic advantages

of the hybrid system: The Cu–Cu_2O/SGr-Bi_2S_3 electrode exhibited a markedly lower Tafel slope of 38 mV·dec^{-1} under CO_2, compared to 67 mV·dec^{-1} for Cu/Cu_2O. Such a reduced Tafel slope points to a more favorable reaction pathway and a lower kinetic barrier for CO_2RR. These results collectively highlight the critical influence of rational catalyst design on CO_2 electroreduction performance. Specifically, the engineered abundance of coordination environments and the expanded electroactive surface area in the Cu–Cu_2O/SGr-Bi_2S_3 hybrid catalyst directly translate to improved activity and selectivity. The distinctive physicochemical properties imparted by SGr-Bi_2S_3 are thus pivotal in accelerating CO_2RR kinetics and enhancing overall catalytic performance.

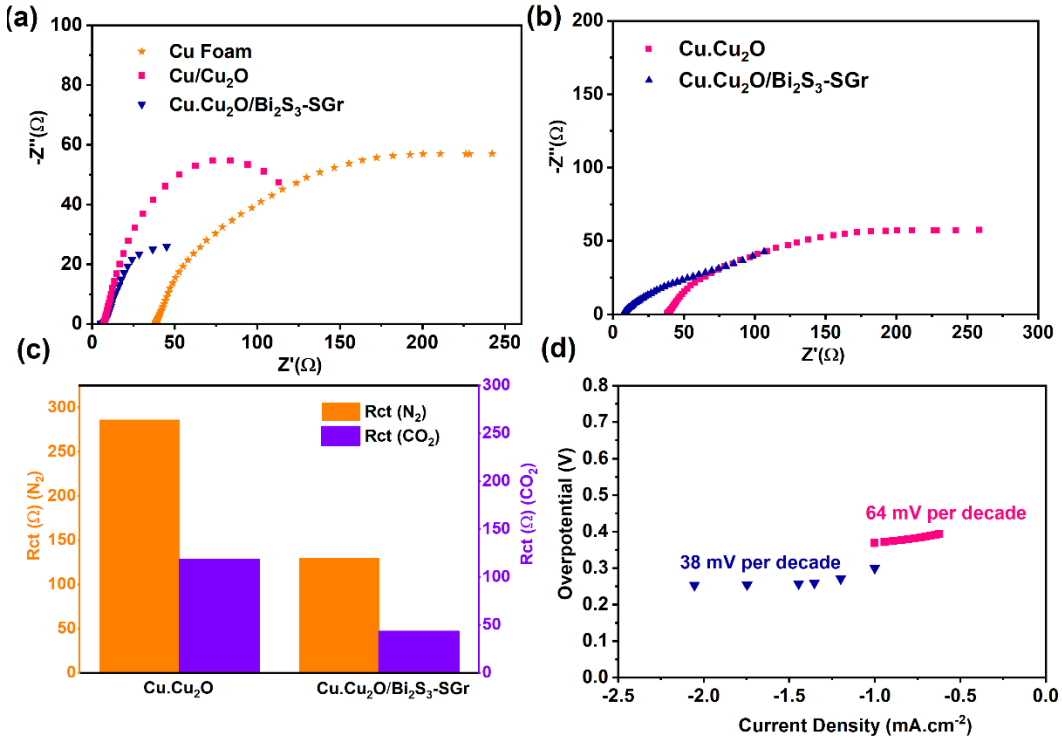

Figure 5. (a) Nyquist plots of various cathodes in CO_2-saturated electrolyte; (b) Nyquist plots in N_2-saturated electrolyte; (c) Fitted electrochemical impedance spectroscopy (EIS) data for the cathodes; (d) Tafel plots for the Cu/Cu_2O and Cu–Cu_2O/SGr-Bi_2S_3 cathodes

Additionally, as illustrated in Figure 4(c), the exchange current density for CO_2 reduction reaction (CO_2RR) is substantially increased when using the Cu-Cu_2O/SGr-Bi_2S_3 catalyst in comparison to pristine Cu-Cu_2O. Under conditions favoring CO_2 reduction, significant competition emerges among CO_2 molecules, bicarbonate ions (HCO_3^-), and water molecules for the available surface-active sites. In this context, the preferential adsorption of CO_2 exclusively occupies these active sites, thereby impeding access for the HER. As a consequence, the activation energy required for HER is elevated, resulting in a marked suppression of its activity. This phenomenon, effectively inhibits the HER as a parasitic side reaction, enabling a significant enhancement in CO_2RR selectivity. Such a mechanism

fundamentally contributes to the enhanced electrochemical performance and selectivity exhibited by the Cu-Cu_2O/SGr-Bi_2S_3 catalyst.

Figure 5(a) further compares current–time profiles for CO_2 reduction across various electrode architectures. Among these, the optimized Cu–Cu_2O/SGr-Bi_2S_3 electrode demonstrated significantly lower current decay compared to the pristine Cu–Cu_2O electrode. During extended electrolysis, it sustained a stable current density of ~10.7 mA cm^{-2}, a durability attributed to the functional groups incorporated into the substrate, which generate a well-tailored surface environment favoring the effective stabilization and utilization of metallic and oxide-based sites. Notably, the Cu/Cu_2O-SGr-Bi_2S_3 electrode exhibited exceptional electrochemical stability, maintaining a nearly constant current density throughout the entire period, underscoring its superior resistance to operational degradation. A particularly noteworthy result is the pronounced change in current density observed in the absence of CO_2 (Figure 5b), which emphasizes the central role of CO_2 reduction in the overall system response. Experimental results confirm that the Cu–Cu_2O/SGr-Bi_2S_3 cathode offers superior resistance to cathodic degradation relative to conventional electrodes. The integration of SGr-Bi_2S_3 into the Cu–Cu_2O matrix not only stabilizes the Cu_2O phase but also significantly enhances both performance and durability, positioning this material as a robust and sustainable catalyst platform for long-term CO_2 electroreduction. As shown in Figure 5b, the current density under a CO_2 atmosphere was approximately twice that observed under N_2, substantiating the high selectivity and pronounced catalytic affinity of the system for CO_2 reduction.

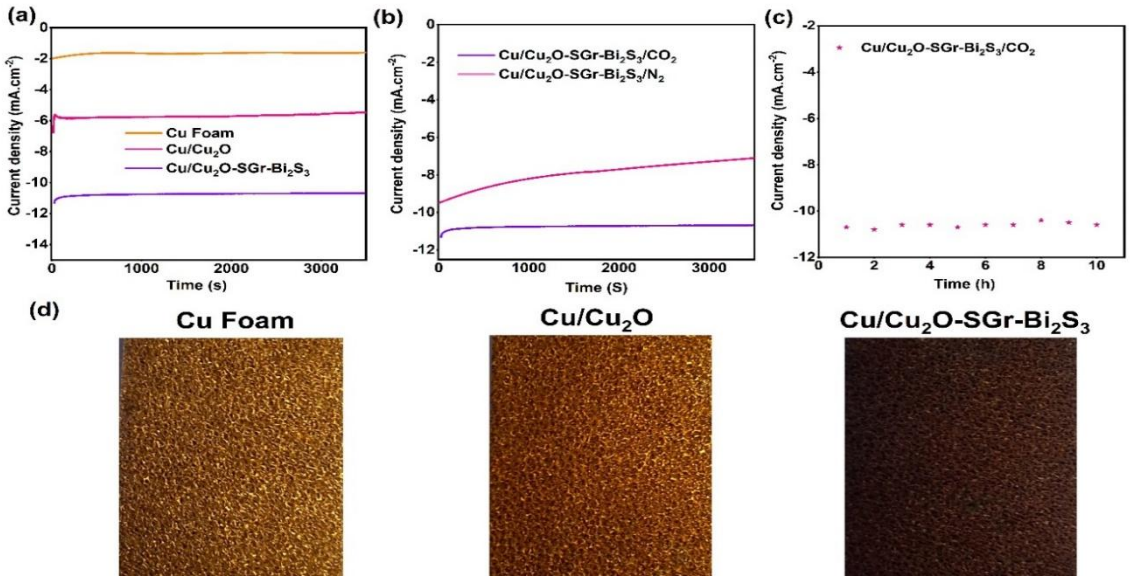

Figure 6. (a) CHA responses of various cathodes in CO_2-saturated $KHCO_3$ electrolyte at –1 V (*vs.* Ag/AgCl); (b) CHA responses of the Cu/Cu_2O-SGr-Bi_2S_3 cathode in CO_2- and N_2-saturated electrolytes; (c) Stability test of the Cu/Cu_2O-SGr-Bi_2S_3 cathode in CO_2-saturated electrolyte at –1 V (vs. Ag/AgCl); and (d) Photograph of the synthesized electrode

To further probe long-term operational stability, the Cu/Cu_2O-SGr-Bi_2S_3 electrode was subjected to continuous electrolysis at –1.0 V for 10 hours (Figure 5 c). Throughout this period, the current density remained closely centered around 10.6 mA cm^{-2}, with negligible fluctuations, further demonstrating the electrocatalyst's outstanding long-term stability [51].

Recent advances show that combining copper oxides with functional materials can enhance both electrode stability and catalytic activity. Table 1 compares the CO_2 reduction performance of various platforms. The Cu/Cu_2O–SGr–Bi_2S_3 system developed here exhibits superior current density, lower charge-transfer resistance, and improved durability over most reported electrodes, underlining the benefit of SGr-Bi_2S_3 integration. Such rational hybrid design enhances catalyst robustness and performance, emphasizing the need for systematic studies of stability and degradation for next-generation CO_2RR electrocatalysts.

Table 1. The comparison of CO_2 reduction performance

Electrode	Applied Potential	Current Density (mA cm^{-2})	R_{ct} (Ω)	Stability	Ref.
PD-Zn/Ag foam	−1.38 V_{RHE}	2.7	-	8 h	[52]
Cu nanodendrites	-1.2 V_{RHE}	10	13.7	7 h	[53]
F-BDD	−1.6 $V_{Ag/AgCl}$	~0.9	~500	50 cycles	[54]
CuZnDTA	−0.63 V_{RHE}	3.4	-	5 h	[55]
Cu/Cu_2O	−2.0 V_{SHE}	7.8	-	50 min	[56]
ZnCuO	−0.8 V_{RHE}	8	-	15 h	[57]
$NtTiO_2$/NsCuO	-1.1 $V_{Ag/AgCl}$	3	1340	-	[58]
CFO/CIS	−0.70 V_{SCE}	1.4	79.89	9 h	[47]
Cu@porphyrin-COFs nanorods	-1 V_{SCE}	~10	78.03	8 h	[59]
Cu/Cu_2O–SGr–Bi_2S_3	-1$V_{Ag/AgCl}$	10.7	43	10 h	This Work

4. CONCLUSION

In this study, we successfully synthesized nanostructured Cu/Cu_2O-modified sulfur-doped graphene/Bi_2S_3 (Cu/Cu_2O–SGr–Bi_2S_3) composites and conducted detailed characterization using FESEM, XRD, and EDS. The Cu_2O nanoparticles were uniformly deposited onto copper substrates via electrophoretic deposition, serving as the working electrode for electrochemical investigations, particularly focused on CO_2 reduction. Electrochemical analyses, including LSV and Tafel slope measurements, demonstrate the promising catalytic activity of the as-fabricated Cu_2O-based electrodes for CO_2 electroreduction reactions (CO_2RR). Notably, the Cu/Cu_2O–SGr–Bi_2S_3 composite enables efficient CO_2 conversion without the need for sacrificial reagents. The integration of SGr–Bi_2S_3 nanoparticles significantly enhances catalytic performance by providing abundant active sites, thereby improving CO_2 adsorption and activation at the catalyst interface. This work highlights the potential of rational design and synergistic integration of Cu_2O with SGr–Bi_2S_3 for superior electrocatalytic efficiency in CO_2

reduction. This strategy addresses the critical need for sustainable chemical processes, offering a viable pathway for converting greenhouse gases into value-added products and contributing to the mitigation of environmental challenges posed by rising atmospheric CO_2 levels.

Acknowledgements

The authors would like to express their gratitude to K. N. Toosi University of Technology, Tehran, Iran, for all support through this project.

Declarations of interest

The authors declare no conflict of interest in this reported work.

REFERENCES

[1] H. Gu, W. Wu, and X.-H. Liu, Diamond and Related Materials 149 (2024) 111544.

[2] H. Ganesha, R. Pavadai, M. Vandana, V.M. Gowri, P. Chanpuang, J. Khumphon, H. Devendrappa, C. Issro, D. Khamboonrueang, S. Kityakarn, and S. Thongmee, Diamond and Related Materials 156 (2025) 112431.

[3] J. Fu, K. Jiang, X. Qiu, J. Yu, and M. Liu, Materials Today 32 (2020) 222-243.

[4] R. Zhang, N. Shehzad, L. Zhang, B. Amin, and I. Shahid, Diamond and Related Materials 139 (2023) 110310.

[5] H.-R.M. Jhong, S. Ma, and P.J.A. Kenis, Current Opinion in Chemical Engineering 2 (2013) 191-199.

[6] B. Qin, S. Jia, P. You, L. Chen, Y. Zhang, Y. Xiong, and P. Zhang, Journal of Electroanalytical Chemistry 965 (2024) 118359.

[7] X. Gu, Y. Jiao, B. Wei, T. Xu, P. Zhai, Y. Wei, J. Zuo, W. Liu, Q. Chen, Z. Yang, F. Zhao, X. Wang, L. Wang, and Y. Gong, Materials Today 54 (2022) 63.

[8] S. Pourebrahimi, M. Pirooz, S. Ahmadi, M. Kazemeini, and L. Vafajoo, Materials Today Physics 38 (2023) 101250.

[9] A. Pandiarajan, G. Hemalatha, B. Mahalakshmi, and S. Ravichandran, Journal of Electroanalytical Chemistry 978 (2025) 118883.

[10] X. Chen, P. Xing, S. Wei, H. Luo, L. Dai, and Y. Wang, Journal of Electroanalytical Chemistry 969 (2024) 118516.

[11] N. Shobanadevi, M.P. Selvi, and N. Kaliyan, Diamond and Related Materials 135 (2023) 109784.

[12] M. Fouladvand, and A. Rouhollahi, International Journal of Hydrogen Energy 133 (2025) 78-90.

[13] P. Kuang, K. Natsui, Y. Einaga, C. Feng, Y. Cui, W. Zhang, and Y. Deng, Diamond and Related Materials 114 (2021) 108310.

[14] T. Kulandaivalu, S. Abdul Rashid, N. Sabli, and T.L. Tan, Diamond and Related Materials 91 (2019) 64.
[15] M. Fouladvand, and A. Rouhollahi, Applied Catalysis B: Environment and Energy 382 (2026) 125983.
[16] M. Gattrell, N. Gupta, and A. Co, Journal of Electroanalytical Chemistry 594 (2006) 1.
[17] D. Karapinar, C.E. Creissen, J.G. Rivera de la Cruz, M.W. Schreiber, and M. Fontecave, ACS Energy Letters 6 (2021) 694.
[18] S. Kreft, D. Wei, H. Junge, and M. Beller, EnergyChem 2 (2020) 100044.
[19] H. Pan, and C.J. Barile, Energy & Environmental Science 13 (2020) 3567.
[20] C. Yang, X. Yu, S. Heißler, A. Nefedov, S. Colussi, J. Llorca, A. Trovarelli, Y. Wang, and C. Wöll, Angewandte Chemie International Edition 56 (2017) 375.
[21] K.P. Kuhl, E.R. Cave, D.N. Abram, and T.F. Jaramillo, Energy & Environmental Science 5 (2012) 7050-7059.
[22] N. Zhang, R. Long, C. Gao, and Y. Xiong, Sci. China Mater 61 (2018) 771.
[23] M. Tarek, K.M. Rezaul Karim, S.M. Sarkar, A. Deb, H.R. Ong, H. Abdullah, C.K. Cheng, and M.M. Rahman Khan, International Journal of Hydrogen Energy 44 (2019) 26271.
[24] A. Navaee, and A. Salimi, Journal of Colloid and Interface Science 505 (2017) 241.
[25] X. Cheng, M. Wu, Y. Xu, S. Wang, D. Wang, W. Wang, N. Mitsuzaki, and Z. Chen, Journal of Solid State Chemistry 338 (2024) 124804.
[26] Y. Zhang, F. Li, X. Zhang, T. Williams, C.D. Easton, A.M. Bond, and J. Zhang, Journal of Materials Chemistry A 6 (2018) 4714.
[27] X.-D. Liang, Q.-Z. Zheng, N. Wei, Y.-Y. Lou, S.-N. Hu, K.-M. Zhao, H.-G. Liao, N. Tian, Z.-Y. Zhou, and S.-G. Sun, Nano Energy 114 (2023) 108638.
[28] J. Yang, X. Wang, Y. Qu, X. Wang, H. Huo, Q. Fan, J. Wang, L.-M. Yang, and Y. Wu, Advanced Energy Materials 10 (2020) 2001709.
[29] L. Zhong, W. Wang, H. Zheng, X. Zeng, F. Guo, L. Shang, and G. Zhan, Molecular Catalysis 580 (2025) 115118.
[30] C. Deacon-Price, N. Chen, A. Lal, P. Broersen, E.J. Meijer, and A.C. Garcia, ChemCatChem 17 (2025) e202401332.
[31] T.H. Phan, K. Banjac, F.P. Cometto, F. Dattila, R. García-Muelas, S.J. Raaijman, C. Ye, M.T.M. Koper, N. López, and M. Lingenfelder, Nano Letters 21 (2021) 2059.
[32] S. Mishra, R.K. Yadav, R. Shahin, K. Sharma, and J.O. Baeg, Diamond and Related Materials (2025) 112604.
[33] L.H.A. Wijewardena, W.S. Cheon, S.-H. Jeong, J. Park, and H.W. Jang, RSC Sustainability (2025).
[34] K.Y. Kumar, M.K. Prashanth, H. Shanavaz, F. Alharethy, B.-H. Jeon, and M.S. Raghu, Diamond and Related Materials 150 (2024) 111740.
[35] G. Wang, X. Shen, B. Wang, J. Yao, and J. Park, Carbon 47 (2009) 1359.

[36] M. Fouladvand, L. Naji, M. Javanbakht, and A. Rahmanian, Journal of Membrane Science 636 (2021) 119563.
[37] S. Kubendhiran, N. Karikalan, S.-M. Chen, P. Sundaresan, and R. Karthik, Journal of Catalysis 367 (2018) 252.
[38] K. Mech, A. Podborska, M. Marzec, K. Szaciłowski, and C.P. de Leon, Sustainable Materials and Technologies 41 (2024) e01000.
[39] T.B. Ferriday, and P.H. Middleton, International Journal of Hydrogen Energy 46 (2021) 18489-18510.
[40] A. Naas, A. Gueddim, B. Khader, O. Meglali, and A. Bouraiou, Physica B: Condensed Matter 711 (2025) 417230.
[41] M. Fouladvand, M. Bayat, and A. Rouhollahi, International Journal of Hydrogen Energy 118 (2025) 14-23.
[42] W. Lv, R. Zhang, P. Gao, and L. Lei, Journal of Power Sources 253 (2014) 276.
[43] X. Huang, Q. Shen, J. Liu, N. Yang, and G. Zhao, Energy & Environmental Science 9 (2016) 3161-3171.
[44] A. Roy, H.S. Jadhav, and J. Gil Seo, Electroanalysis 33 (2021) 705.
[45] S. Mena, E. Ribas, C. Richart, I. Gallardo, J. Faraudo, S.K. Shaw, and G. Guirado, Journal of Electroanalytical Chemistry 895 (2021) 115411.
[46] P.K. Jiwanti, A.M. Ichzan, R.K.P. Dewandaru, S.R. Atriardi, Y. Einaga, and T.A. Ivandini, Diamond and Related Materials 106 (2020) 107874.
[47] J. Yuan, C. Gu, W. Ding, and C. Hao, Energy & Fuels 34 (2020) 9914.
[48] M. Hedayati, M. Fouladvand, and A. Rouhollahi, International Journal of Hydrogen Energy 84 (2024) 288-295.
[49] D. Voiry, M. Chhowalla, Y. Gogotsi, N.A. Kotov, Y. Li, R.M. Penner, R.E. Schaak, and P.S. Weiss, ACS Nano 12 (2018) 9635.
[50] J. Chen, Z. Wang, H. Lee, J. Mao, C.A. Grimes, C. Liu, M. Zhang, Z. Lu, Y. Chen, S.P. Feng, Materials Today Physics 12 (2020) 100176.
[51] Y. Zhang, D. Pan, Y. Tao, H. Shang, D. Zhang, G. Li, and H. Li, Advanced Functional Materials 32 (2022) 2109600.
[52] Q.H. Low, N.W.X. Loo, F. Calle-Vallejo, and B.S. Yeo, Angewandte Chemie International Edition 58 (2019) 2256.
[53] M. Wu, C. Zhu, K. Wang, G. Li, X. Dong, Y. Song, J. Xue, W. Chen, W. Wei, and Y. Sun, ACS Applied Materials & Interfaces 12 (2020) 11562.
[54] D. Luo, D. Ma, S. Liu, K. Nakata, A. Fujishima, and L. Wu, Diamond and Related Materials 121 (2022) 108753.
[55] J. Albo, D. Vallejo, G. Beobide, O. Castillo, P. Castaño, and A. Irabien, ChemSusChem 10 (2017) 1100.
[56] J. Hazarika, and M.S. Manna, Electrochimica Acta 328 (2019) 135053.

[57] M.H. Suliman, H. Al Naji, and M. Usman, Electrochimica Acta 500 (2024) 144723.
[58] J.F.d. Brito, F.F. Hudari, and M.V.B. Zanoni, Journal of CO2 Utilization 24 (2018) 81.
[59] B. Wang, F. Yang, Y. Dong, Y. Cao, J. Wang, B. Yang, Y. Wei, W. Wan, J. Chen, and H. Jing, Chemical Engineering Journal 396 (2020) 125255.